Journal of Inorganic Biochemistry 256 (2024) 112565

Contents lists available at ScienceDirect

Journal of Inorganic Biochemistry

journal homepage: www.elsevier.com/locate/jinorgbio

Role of second-sphere arginine residues in metal binding and metallocentre assembly in nitrile hydratases

Callie Miller [a], Delanie Huntoon [b], Nicholas Kaley [c], Irene Ogutu [a], Adam T. Fiedler [b], Brian Bennett [d], Dali Liu [c], Richard Holz [a,*]

[a] Department of Chemistry and Geochemistry, Colorado School of Mines, Golden, CO 80401, USA
[b] Department of Chemistry, Marquette University, Milwaukee, WI 53233, USA
[c] Department of Chemistry and Biochemistry, Loyola University, Chicago, IL 60660, USA
[d] Department of Physics, Marquette University, Milwaukee, WI 53233, USA

ARTICLE INFO

Keywords:
Nitrile hydratase
Cobalt
electron paramagnetic resonance
X-ray crystallography
Mutagenesis
Second sphere residues

ABSTRACT

Two conserved second-sphere βArg (R) residues in nitrile hydratases (NHase), that form hydrogen bonds with the catalytically essential sulfenic and sulfinic acid ligands, were mutated to Lys and Ala residues in the Co-type NHase from *Pseudonocardia thermophila* JCM 3095 (*Pt*NHase) and the Fe-type NHase from *Rhodococcus equi* TG328–2 (*Re*NHase). Only five of the eight mutants (*Pt*NHase βR52A, βR52K, βR157A, βR157K and *Re*NHase βR61A) were successfully expressed and purified. Apart from the *Pt*NHase βR52A mutant that exhibited no detectable activity, the k_{cat} values obtained for the *Pt*NHase and *Re*NHase βR mutant enzymes were between 1.8 and 12.4 s^{-1} amounting to <1% of the k_{cat} values observed for WT enzymes. The metal content of each mutant was also significantly decreased with occupancies ranging from ~10 to ~40%. UV–Vis spectra coupled with EPR data obtained on the *Re*NHase mutant enzyme, suggest a decrease in the Lewis acidity of the active site metal ion. X-ray crystal structures of the four *Pt*NHase βR mutant enzymes confirmed the mutation and the low active site metal content, while also providing insight into the active site hydrogen bonding network. Finally, DFT calculations suggest that the equatorial sulfenic acid ligand, which has been shown to be the catalytic nucleophile, is protonated in the mutant enzyme. Taken together, these data confirm the necessity of the conserved second-sphere βR residues in the proposed subunit swapping process and post-translational modification of the α-subunit in the α activator complex, along with stabilizing the catalytic sulfenic acid in its anionic form.

1. Introduction

Nitrile hydratases (NHase, EC 4.2.1.84) catalyze the conversion of nitriles to amides at ambient temperature and pressure, a marked improvement over the harsh industrial reaction conditions for amide production (either acid or base hydrolysis) that are often incompatible with the sensitive structures of many industrially and synthetically relevant compounds [1,2]. NHases are metalloenzymes that contain either a low spin ($S = 0$) non-corrin Co(III) ion (Co-type) or a low spin ($S = 1/2$) non-heme Fe(III) ion (Fe-type) in the active site [2]. All crystallographically characterized prokaryotic NHases are $\alpha_2\beta_2$-heterotetramers with a strictly conserved metal binding site located in the α-subunit, where the metal ion is coordinated by three cysteine residues, two backbone amide nitrogen atoms, and a water molecule [2]. The two equatorial cysteine ligands are post-translationally modified to Cys-sulfinic (-SO_2(H); CSD) acid and Cys-sulfenic (-SO(H); CSO) acid, both of which are catalytically essential [2]. There are various, conflicting proposals regarding the protonation states of the sulfenic and sulfinic acid ligands; however, the most recent work suggests that both are deprotonated in the catalytically active enzyme, with the sulfenic acid ligand functioning as the nucleophile in catalysis [3–5].

Downstream from the structural α/β subunit genes is an activator (ε) protein gene that is required for nearly all NHases to be fully metalated and post-translationally modified [6]. While the NHase $\alpha_2\beta_2$-heterotetramers are quite similar between Fe- and Co-type NHases, the ε proteins differ in size and sequence identity, suggesting that Fe- and Co-type NHases may have different mechanisms of metalation and post-translational modification. Fe-type ε proteins are ~45 kDa with a known metal binding motif and GTPase activity [49]. On the other hand, the Co-type ε proteins are much smaller (~17 kDa) and do not have any

* Corresponding author at: Department of Chemistry, Colorado School of Mines, Golden, CO 80401, USA.
E-mail address: rholz@mines.edu (R. Holz).

https://doi.org/10.1016/j.jinorgbio.2024.112565
Received 9 February 2024; Received in revised form 7 April 2024; Accepted 13 April 2024
Available online 16 April 2024

known metal binding motifs, but can function as an ATPase [2,7,8]. In 2008, Zhou et al. proposed a heretofore unknown 'subunit swapping' mechanism for the Co-type NHase from *Pseudonocardia thermophila* JCM 3095 (*Pt*NHase), where the $\alpha_2\beta_2$-complex first forms as the apo-tetramer while a single α-subunit binds to two Co(II)-containing ε proteins to form an $\alpha\varepsilon_2$ complex [9]. It was proposed that after insertion of a Co(II) ion into the α-subunit of the $\alpha\varepsilon_2$ complex, the cobalt and equatorial cysteines are oxidized to their sulfenic and sulfinic acid states, after which the now functional α-subunits are swapped for apo-α-subunits in the apo-$\alpha_2\beta_2$-heterotetramer to produce the functional tetrameric protein (Fig. S1) [9–11].

Although not much is known about *how* this subunit swapping process occurs, it is essential to NHase metallocentre assembly and active site post-translational modification [8,9]. One hypothesis is that a salt bridge forms between two highly conserved positively charged second-sphere βArg (R) residues and the negatively charged active site equatorial sulfenic/sulfinic acid ligands [9]. Based on X-ray crystallography, these two second-sphere βR residues form hydrogen bonds to the sulfenic and sulfinic acid ligands, also suggesting a role in catalysis. Previously, one of these βR residues was mutated to Lys (K), Tyr (Y), and Glu (E) in an Fe-type NHase; however, only the K mutant retained any detectable catalytic activity (~1%) [12]. Herein, we report the mutation of each of these conserved second-sphere arginine residues: βR52 and βR157 in *Pt*NHase and βR61 and βR146 in the Fe-type NHase from *Rhodococcus equi* TG328–2 (*Re*NHase), to Ala (A) and K residues. Both the *Pt*NHase and *Re*NHase mutant enzymes were characterized kinetically and spectroscopically; these data, coupled with DFT calculations and X-ray crystal structures of the *Pt*NHase mutants, provide new insights into both the catalytic mechanism of NHases and the proposed subunit swapping process [8,13–16].

2. Materials and methods

2.1. Materials

All reagents were purchased commercially at the highest purity available. Isopropyl-β-D-1-thiogalactopyranoside (IPTG), 4-(2-hydroxyethyl)-1-piperazineethanesulfonic acid (HEPES), tris(hydroxymethyl) aminomethane hydrochloride (Tris-HCl), sodium citrate tribasic, glycerol, Luria-Bertani (LB) broth, agar, nitric acid, hydrochloric acid, butyric acid, acetonitrile, acrylonitrile, kanamycin, ampicillin, carbenicillin, imidazole, cobalt chloride, and sodium chloride were all purchased from either Sigma Aldrich or Thermo Fisher scientific. Pre-cast polyacrylamide gel electrophoresis (PAGE) gels, SDS and native PAGE running buffers, sample buffers and ladders were purchased from Bio-Rad Laboratories. NEB and BL21(DE3) *E. coli* competent cells and mutagenesis kits (QuikChange) were purchased from Agilent Technologies, and plasmid purification kits were purchased from Promega. 5 mL IMAC Ni-NTA purification columns were purchased from Qiagen.

2.2. Mutagenesis

The α- and β-subunits of *Pt*NHase were previously inserted into a pET-28a(+) vector with a hexahistidine tag on the C-terminus of the α-subunit [17]. Similarly, the *Re*NHase α- and β-subunits were inserted into the pET-28a(+) vector with two hexahistidine tags: one on the N-terminus of the α-subunit and the other on the C-terminus of the β-subunit [18]. Both the *Pt*NHase and *Re*NHase wild type (WT) α/β sequences were used for mutagenic primer design using SnapGene and Integrated DNA Technologies Inc. The forward primer sequences are listed below and used with complementary reverse primer sequences.

- 5'-GACGAGTTCaagTTCGGCATCGAG-3' *Pt*NHase βR52K
- 5'-GACGAGTTCgcgTTCGGCATC-3' *Pt*NHase βR52A
- 5'-CACGCCaagCGCGCGCGGTAC-3' *Pt*NHase βR157K
- 5'-AAGGGCCACGCCgcaCGCGCGCGGTACGT-3' *Pt*NHase βR157A
- 5′- GTCGACGAGGTCaagCACGTCGTCGAACGC-3' *Re*NHase βR61K
- 5′- TTCAGTGTCGACGAGGTCgctCACGTCGTCG-3' *Re*NHase βR61A
- 5′- CGTGACGAGTTCTTCGCCGGACACATTaagATGCCTGCGTACTGC CGCGGT-3' *Re*NHase βR146K
- 5′- TTCGCCGGACACATTgcgATGCCTGCGTAC-3' *Re*NHase βR146A

Using the polymerase chain reaction (PCR) and the QuikChange site directed mutagenesis kit (Agilent), the bases in lowercase letters were changed in the WT β-subunit of *Pt*NHase or *Re*NHase. The forward and reverse primers were used to perform two half PCR reactions, and then mixed for another PCR reaction to produce the fully mutated plasmid. The mutant plasmids were transformed into *XL10-Gold* Ultracompetent cells, plated, and grown overnight on LB media. The Promega Wizard SV genomic DNA purification kit was used according to the corresponding protocol to produce plasmids, and mutations were confirmed via sequencing (Azenta).

2.3. Transformation, growth, harvesting, and storage

The plasmids for the mutated α- and β-subunits of *Pt*NHase (pET-28a(+)) and the necessary ε protein (pET-21a(+)) were co-transformed into BL21(DE3) cells and plated on carbenicillin (100 μg/mL)/kanamycin (50 μg/mL) agar plates. The same protocol was followed for the mutated α- and β-subunits of *Re*NHase (pET-21a(+)) and ε protein (pET-28a(+)). For each mutant, a single colony was used to inoculate 100 mL of LB broth with 50 μg/mL kanamycin and 100 μg/mL ampicillin and grown overnight at 37 °C with shaking (200 rpm). These starter cultures were used to inoculate 8 L of LB broth with 50 μg/mL kanamycin and 100 μg/mL ampicillin. Cells were grown at 37 °C and 200 rpm until an optical density at 600 nm of ~0.8–1.0 was reached. The cultures expressing mutant enzymes were induced with 0.1 mM isopropyl-β-D-1-thiogalactopyranoside (IPTG), cooled to 20 °C and shaken at 200 rpm for an additional 16 h. Upon induction, 0.25 mM cobalt chloride was added to the *Pt*NHase cultures. Cells were pelleted by centrifugation at 7000 rpm for 15 min and resuspended in 50 mM HEPES with 500 mM NaCl at pH 7.5. Cell paste was stored at −80 °C until purification.

2.4. Purification of mutant PtNHase and ReNHase

The resuspended cell pastes for each *Pt*NHase and *Re*NHase mutant enzyme were thawed and lysed on ice by ultrasonication (Misonix Sonicator 300 with microtip) in 30 s increments for 20 min at 21 W. The lysate and cell debris were separated by centrifugation at 16,000 rpm for 40 min., and supernatant was collected. Buffers A and B were prepared: (A) 50 mM HEPES, 500 mM NaCl at pH 7.5 and (B) 50 mM HEPES, 500 mM NaCl, 500 mM imidazole at pH 7.5 and filtered through a 0.22 μm nitrocellulose membrane. Additionally, *Re*NHase purification requires the addition of 40 mM butyric acid to buffer B to slow the oxidation of the enzyme active site, as previously described [14]. The supernatant containing expressed mutant enzyme was loaded onto a Qiagen IMAC Ni-NTA column that was pre-equilibrated with buffer A. The column was washed with 20 column volumes (CV) of buffer A with 4% buffer B, and subsequently washed with 20 CV of buffer A with 10% buffer B. The protein of interest was eluted with a wash gradient of 60 mL from 10% B to 60% B. Fractions were collected and loaded into a 30 kDa Amicon centrifugation tube where the protein was buffer exchanged back into buffer A and concentrated to a volume of <1 mL. Each purified mutant protein was stored in aliquots at −80 °C until ready for experimental use. Most of the *Re*NHase mutants did not bind to the Ni-NTA column as they appeared as inclusion bodies, thus, only the βR61A mutant was successfully purified (identity confirmed through SDS-PAGE and circular dichroism (CD)). Native PAGE gels were run on each mutant enzyme with non-denatured samples (prepared with Native Sample Buffer from Bio-Rad) in a Tris/Glycine buffer without SDS.

2.5. Steady-state kinetic assays

The enzymatic activity of NHase utilized acrylonitrile as the substrate and was monitored through product formation at 225 nm (acrylamide; $\Delta\varepsilon_{225} = 2.9\ mM^{-1}\ cm^{-1}$) on an Agilent 8453 UV–visible spectroscopy system with an Agilent 89090 A Peltier temperature-controlled cell holder. Enzyme was added to a 1 mL quartz cuvette containing 50 mM Tris-HCl pH 7.5 at 25 °C. Acrylonitrile concentrations ranged from 0.5 to 480 mM with protein concentrations ranging 100–200 nM. Kinetic parameters k_{cat} and K_M were obtained by fitting these data to the Michaelis-Menten equation using the OriginPro9.0 software (OriginLab) (Table 1).

2.6. Metal analysis, circular dichroism, and electronic absorption spectroscopy

The metal contents of each mutant were determined via inductively coupled plasma atomic emission spectroscopy (ICP-AES) and inductively coupled plasma mass spectrometry (ICP-MS). Each sample was first denatured for 4 h at room temperature with 200 mL of 8 M urea, followed by overnight denaturation with trace metal grade 2% nitric acid and 0.5% hydrochloric acid *v*/v mixture to a final volume of 10 mL. Denatured samples were centrifuged and run through a 0.2 μm filter to remove precipitation before ICP-AES/ICP-MS analysis (Table 1). The WT *Re*NHase and *Re*NHase mutant enzymes were concentrated to 0.5 mg/mL and buffer exchanged into a 20 mM sodium phosphate to collect circular dichroism (CD) spectra. Spectra were collected in a 0.5 mm quartz cuvette on an Applied Photophysics Chirascan Plus CD with a Peltier temperature-controlled cell held at 25 °C. Data analysis was performed using the online software DichroWeb, using the analysis program CONTIN with reference set SMP180 [19]. Each mutant enzyme was concentrated to 300 μM and UV–Vis spectra were collected in 50 mM HEPES buffer, pH 7.5 at 25 °C in a 1 cm quartz cuvette on an Agilent 8453 UV–visible spectroscopy system with an Agilent 89090 A Peltier temperature-controlled cell holder.

2.7. Electron paramagnetic resonance (EPR) spectroscopy

X-band EPR spectra were collected for both WT *Re*NHase and the βR61A mutant *Re*NHase enzymes on a Bruker EMX-AA-TDU/L spectrometer. Experimental spectra were recorded at 77 K in a liquid nitrogen cooling system centered around 9.44 GHz with 5 mW microwave power. Spectral analysis and simulations were performed using EasySpin [20,21].

2.8. Computational Methods

Active-site models for computational studies of Fe-type NHase [22,23], were derived from the X-ray structure of the Fe-type NHase from *Re*NHase-TG328–2 [23]. Constrained geometry optimizations were performed using unrestricted density functional theory (DFT), as implemented in the ORCA 4.0 software package [24,25]. These calculations utilized the PBE0 functional (i.e., the one-parameter hybrid version of the Perdew-Burke-Ernzerhof functional) and the valence triple-ζ Karlsruhe basis with polarization functions on main-group and transition-metal elements (def2-TZVP) [26–28]. This combination of functional and basis set provided accurate geometries in our earlier studies of Fe-type NHase [22,23]. Fig. S2 illustrates the size and scope of the active-site models examined here, with positions of atoms marked with asterisks belonging to the protein backbone. These positions were fixed during geometry optimizations. For the WT *Re*NHase enzyme, models included the two conserved arginine residues (βR61 and βR146) that form hydrogen bonds to the αCSO118 and αCSD116 ligands. The position *trans* to the axial Cys donor is occupied by either H_2O or CH_3CO_2H; the latter is a truncated version of butyric acid. Models of the βR61A variant were prepared by removing the second-sphere βR61 residue in silico. Because this residue is positively charged, its removal results in an active site with an overall −1 charge. Neutral models in which the αCSO118 ligand is protonated were also generated for the βR61A variant, along with structures that feature an adventitious H_2O molecule in the space formerly occupied by βR61, as suggested by one of the X-ray structures of Co-type *Pt*NHase (βR52Ala). Each of the structural models was subjected to constrained DFT geometry optimization.

EPR *g*-values for $S = 1/2$ NHase models were calculated using three different methodologies, and the results are summarized in Table S1. The application of coupled-perturbed SCF (CP-SCF) equations to DFT calculations [29,30] yielded *g*-values in generally poor agreement with experiment, as the computed g_3-values are all >2.0 (instead of below 2.0, as is typical for low-spin Fe(III) ions). We therefore pursued a multiconfigurational approach, referred to here as quantum chemical theory (QCT), that pairs complete active space self-consistent field (CASSCF) calculations with *N*-electron valence perturbation theory (NEVPT2) [31,32]. Although this combination has provided accurate *g*-values for a number of low-spin Fe(III) systems [32,33], our previous study of *Re*NHase found that it greatly overestimates the *g*-anisotropy of Fe-type NHase models [22]. Those earlier calculations employed the minimal CAS(5,5) active space consisting of five electrons in the five iron 3d orbitals. Here, we expanded the active space to CAS(11,13) to better account for metal-ligand covalency and radial correlation. A minimum of five doublet states were calculated. Because the results of CASSCF/NEVPT2 calculations exhibit only minor basis set dependence, the CAS(11,13) calculations employed the smaller valence double-zeta Karlsruhe basis set with polarization (def2-SVP). Expanding the active site to CAS(11,13) significantly improved agreement with experiment; however, the g_1-values are still overestimated by approximately 0.15 for WT *Re*NHase models. Improved results were obtained via a combined approach (henceforth referred to as QCT/Taylor), that employed ab initio CASSCF/NEVPT2 calculations to compute the relative energies of the three lowest energy ligand-field states, which are derived from the parent $^2T_{2g}$ state in octahedral symmetry. These energies were then used to calculate EPR *g*-values by applying the set of equations derived originally by Taylor for low-spin Fe(III) systems [34,35]. Calibration of this method using a synthetic nonheme Fe-S/N complex with known *g*-values provided an optimal spin-orbit coupling parameter (ζ) of 400

Table 1
Kinetic constants (k_{cat} and K_M) for WT and mutant *Pt*NHase and *Re*NHase with acrylonitrile as substrate in 20 mM Tris-HCl at pH 7.5 and 25 °C, and metal concentration in soluble protein (ICP-MS and ICP-AES), where M^{3+} is cobalt for *Pt*NHase and iron for *Re*NHase.

	k_{cat} (s^{-1})	K_M (mM)	k_{cat}/K_M ($s^{-1}\ mM^{-1}$)	% activity	M^{3+} eq.
WT *Pt*NHase	1600 ± 120	7 ± 1	300	100%	2.0 ± 0.1
*Pt*NHase βR157A	1.8 ± 0.1	3.1 ± 0.4	0.6	0.11%	0.4 ± 0.1
*Pt*NHase βR157K	12.4 ± 0.1	6.0 ± 0.8	2.1	0.78%	0.2 ± 0.1
PtNHase βR52A	nd*	nd*	nd*	nd*	0.4 ± 0.1
*Pt*NHase βR52K	4 ± 1	77 ± 9	0.1	0.25%	0.4 ± 0.2
WT *Re*NHase	1300 ± 200	31 ± 1	42	100%	2.0 ± 0.1
*Re*NHase βR61A	3.9 ± 0.1	4.0 ± 0.9	1.0	0.30%	0.8 ± 0.1

nd* = none detected.

Table 2
Refinement and data collection statistics for each *Pt*NHase mutant crystal structure.

Data Set	βR157A	βR157K	βR52A	βR52K
Space Group	$P3_221$	$P3_221$	$P3_221$	$P3_221$
Cell Dimensions				
a = b (Å)	66.176	65.91	65.964	65.895
c (Å)	185.671	184.28	186.400	184.943
α = β (°)	90	90	90	90
γ (°)	120	120	120	120
Resolution (Å)	19.47–1.29	19.54–1.56	31.09–1.45	19.55–1.47
R_{merge}	0.070 (0.491)	0.067 (0.737)	0.168 (0.967)	0.066 (0.932)
R_{pim}	0.023 (0.262)	0.019 (0.286)	0.055 (0.336)	0.021 (0.291)
I/sigma	15.7 (2.1)	20.6 (2.2)	8.8 (2.1)	18.4 (2.2)
Completeness (%)	99.87 (99.17)	99.91 (99.85)	99.37 (100.00)	98.79 (98.18)
Multiplicity	9.3 (4.3)	13.1 (7.2)	10.5 (9.1)	10.8 (11.0)
No. Total reflections	1,112,253 (25044)	886,773 (24242)	888,880 (38180)	857,926 (42437)
No. Unique reflections	119,354 (11701)	67,059 (6604)	83,861 (8359)	79,255 (7759)
R_{work}	0.1647 (0.2647)	0.1694 (0.2403)	0.2473 (0.3349)	0.1955 (0.2803)
R_{free}	0.1896 (0.2984)	0.1913 (0.2780)	0.2663 (0.3500)	0.2279 (0.3251)
Twin Law	None	None	-h,-k,l	None
No. of Atoms	4241	4183	4007	4059
No. of Solvent Atoms	713	670	468	550
B-factors (Å^2)				
Overall	21.48	27.71	18.15	27.09
Protein	19.09	25.98	17.20	25.41
Water	33.31	36.74	25.33	37.83
RMSD Bond Length (Å)	0.012	0.005	0.002	0.004
RMSD Bond Angles (°)	1.24	0.83	0.49	0.75
Ramachandran				
Favored (%)	98.10	97.41	97.64	97.64
Allowed (%)	1.90	2.59	2.36	1.65
Outlier (%)	0.00	0.00	0.00	0.71

cm^{-1} [36]. Computed *g*-values were required to correspond to a normalized singly occupied 3d orbital. The combined Taylor/QCT approach reduces the gap between the computed and experimental g_1-values to 0.07 or less for WT species (Table S1), and the overall agreement for the three *g*-values is excellent (root-mean-square deviation of 0.02–0.04).

2.9. Crystallization and X-ray data collection

Crystallizations of the *Pt*NHase mutant enzymes were performed using a sitting drop protocol of 20 mg/mL protein solution mixed with a well solution consisting of 1.2 M sodium citrate tribasic in 0.1 M HEPES at pH 7.5, as previously reported [2,37]. Diffraction quality crystals grew within two weeks and upon harvesting, were submerged in cryoprotectant containing 20% glycerol (*v*/v), flash frozen, and stored in liquid nitrogen. Diffraction data were collected at beamline 21-ID-G of the Advanced Photon Source at Argonne National Laboratory. The beamline was equipped with a MAR 300 Charged Coupled Device (CCD). Data were collected using an oscillation angle of 0.5° over a range of 180° and an exposure time of 1.0 s per frame. The wavelength was fixed at 0.97856 Å. Data processing and reduction, including indexing, integration, and scaling was done using the autoPROC software [38]. Data processing and refinement statistics are summarized in Table 2. The *Pt*NHase structures were solved via molecular replacement using PHASER within the Phenix software suite [39,40]. The initial search model included the previously published WT *Pt*NHase (PDB: 1IRE). Model building and subsequent refinement was performed using COOT and PHENIX.REFINE respectively [40]. Structural figures were made using UCSF Chimera [41].

3. Results and discussion

Two strictly conserved arginine (R) residues on the β-subunit of prokaryotic NHases (Table S2) form hydrogen bonds with the active site sulfenic and sulfinic acid ligands (Fig. 1) [2]. These residues are βR52 and βR157 in *Pt*NHase and βR61 and βR146 in *Re*NHase [2,42]. In all NHases, the equivalent βR residue to βR52 in *Pt*NHase forms a hydrogen bond to both the sulfenic-αCSO113 ligand and the sulfinic-αCSD111 ligand (αCSO118 and αCSD116 in *Re*NHase), while the equivalent of βR157 forms two hydrogen bonds to the sulfinic-αCSD111 ligand (Fig. 1) [9,10,12]. It was hypothesized that the function of these βR residues is two-fold: (i) they form a salt bridge between the β-subunit and the α-subunit in the $\alpha\varepsilon_2$ complex to facilitate α-subunit swapping and (ii) likely play a role in catalysis through hydrogen bond formation to the active site sulfinic and sulfenic acid ligands, the latter of which is proposed to function as a nucleophile towards the nitrile substrate. In an effort to gain insight into the roles of these two conserved βR residues in NHase maturation and catalysis, both were mutated to K and A residues.

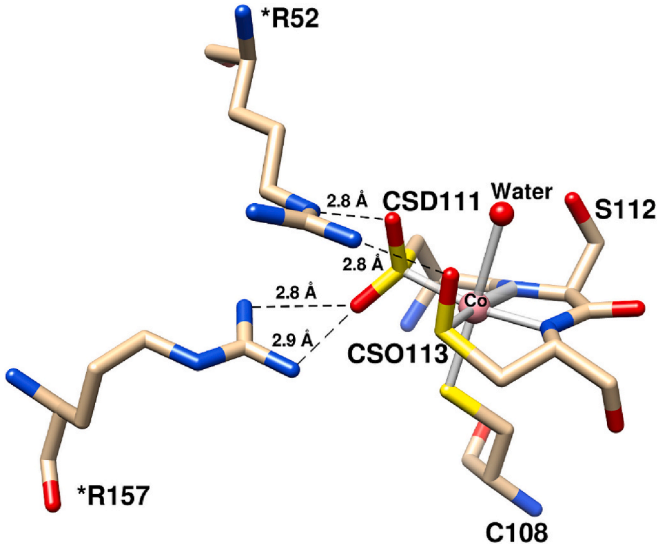

Fig. 1. Active site of WT *Pt*NHase (PDB: 1IRE). Residues that are from the β-subunit are denoted with an *. Key distances in proposed salt bridges are shown in Å.

3.1. Purification, kinetic, and metal analysis

The *Pt*NHase βR52A, βR52K, βR157A, and βR157K mutants were successfully expressed and purified, providing colorless samples. On the other hand, three of the *Re*NHase Fe-type mutants (βR61K, βR146K, and βR146A) formed inclusion bodies and could not be refolded. Therefore, only the βR61A *Re*NHase mutant enzyme was purified and exhibited a light green color. CD spectra of the *Re*NHase βR61A mutant enzyme display α-helix (~18%) and β-sheet (~31%) content similar to WT *Re*NHase, which exhibits ~20% α-helix and ~30% β-sheet content. Both enzymes contain ~50% random coil content (Fig. S3). These data indicate that the *Re*NHase βR61A enzyme is folded properly.

The metal content of each mutant was determined through both ICP-AES and ICP-MS and the data from both methods were in good agreement (Table 1). As expected, WT *Pt*NHase and *Re*NHase had ~2 eqs. of metal per tetramer, however, each of the five mutants displayed <2 eqs. of metal. The *Pt*NHase βR52A, βR52K and βR157A mutants each contained ~0.4 eqs. of cobalt per tetramer, while the *Pt*NHase βR157K mutant enzyme had only ~0.2 eqs. On the other hand, the *Re*NHase βR61A mutant enzyme contained ~0.8 eq. of iron per tetramer (Table 1). As the metal concentration for *Pt*NHase ranged from 10% to 20% while the *Re*NHase mutant contained only ~40% of the WT metal content, mutation of the second-sphere βR residues clearly impacts the ability of the active sites to incorporate metal ions, suggesting that these βR residues may indeed play a role in the subunit swapping process.

The catalytic constants for WT and mutant NHases are presented in Table 1. The *Pt*NHase mutants exhibited 0–0.8% of the catalytic activity observed for WT *Pt*NHase, while the βR61A *Re*NHase mutant exhibited only 0.3% of WT activity. As a result of the decreased k_{cat} values, the catalytic efficiency (k_{cat}/K_M) for each mutant enzyme examined decreased ~100-fold for *Pt*NHase and ~ 42-fold for *Re*NHase (Table 1). As the substrate binds directly to the metal center, the diminished catalytic efficiency is not simply due to incomplete maturation of the enzyme. The k_{cat} and K_M values relate to the remaining, small fraction of metalated enzyme as there are no known secondary substrate binding partners and catalysis is unlikely in the apo- form of the enzyme. For the *Pt*NHase βR157A and βR157K mutant enzymes, the K_M values were not distinguishable from those of WT *Pt*NHase, but interestingly, the *Pt*NHase mutant, βR52K mutant enzyme, exhibited a K_M value approximately an order of magnitude greater than that of WT *Pt*NHase. One explanation is that an increase in electron density on the metal center after the loss of the βR52 hydrogen bond diminishes the Lewis acidity of the Co(III) ion. A previous investigation of the βR61K mutant in an Fe-type NHase reported <1% activity towards methacrylonitrile with a K_M an order of magnitude less than WT NHase [12]. For the *Re*NHase βR61A mutant, its observed K_M is also an order of magnitude less than that of WT *Re*NHase. Collectively, the metal binding and kinetic data indicate that the second-sphere βR residues not only impact the ability of the NHase active sites to catalytically hydrate nitriles to amides, but also play a role in the ability of the α-subunit to incorporate metal ions. These conclusions are consistent with the proposal that these βR residues may play a role in the subunit swapping mechanism.

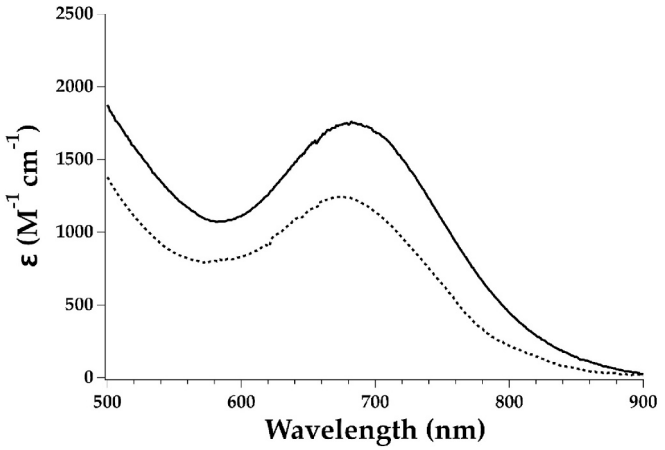

Fig. 2. Absorption spectra from 400 to 900 nm of WT *Re*NHase (solid trace) and *Re*NHase βR61A (dashed trace).

3.2. Electronic absorption and electron paramagnetic resonance spectroscopy

The UV–Vis spectrum of WT *Pt*NHase exhibited a characteristic band at 320 nm due to an axial thiolate S(π)-to-Co(III) charge transfer (CT) transition. As a result, the sample exhibited an observable tan (straw) color [16,43]. All four *Pt*NHase βR mutant enzymes were colorless and had no observable ligand-to metal CT (LMCT) band (Fig. S4). The loss of this LMCT band is most likely the result of low Co(III) content in each mutant enzyme; however, no absorption was observed even at high enzyme concentrations (~1 mM). The UV–Vis spectrum of the *Re*NHase βR61A mutant enzyme exhibited an absorption band at 680 nm, assigned to an axial thiolate (S → Fe(III)) LMCT. This band is blue shifted by ~20 nm with respect to the corresponding peak in the WT *Re*NHase spectrum (Fig. 2). This observation is in good agreement with previous

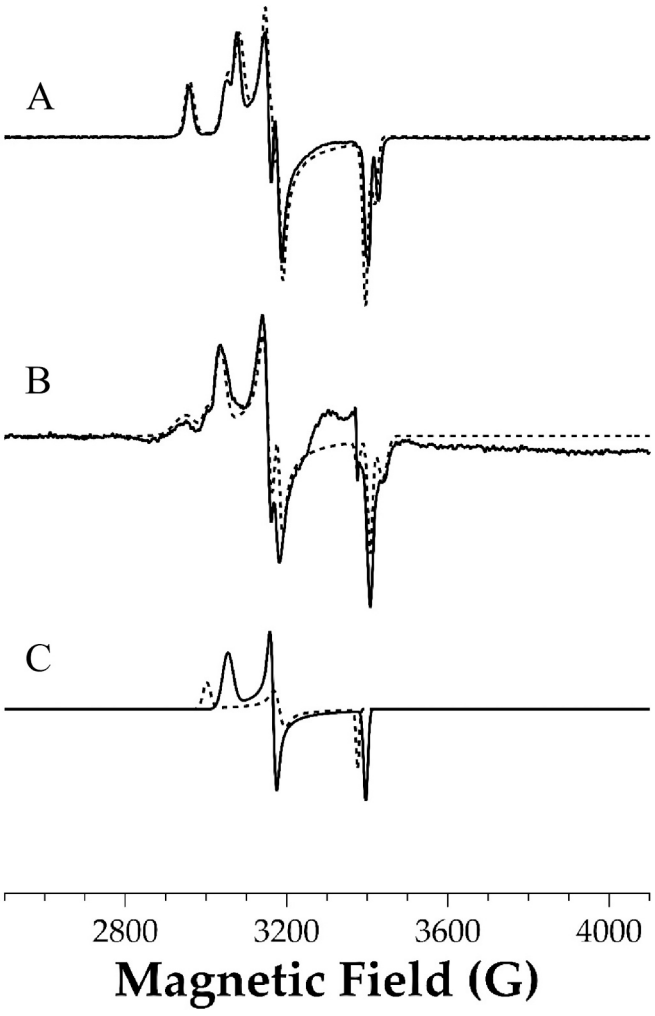

Fig. 3. A. Simulated EPR spectrum of WT *Re*NHase (dashed trace) overlaid on the experimental EPR spectrum of WT *Re*NHase with butyric acid (solid trace). **B.** Simulated EPR spectrum of *Re*NHase βR61A (dashed trace) overlaid on the experimental EPR spectrum of *Re*NHase βR61A with butyric acid. **C.** Isolated simulation species of WT *Re*NHase^{Aq} (solid trace) and βR61A *Re*NHase^{Aq} (dashed trace) where βR61A is shifted upfield by $\delta g \approx 0.04$.

Table 3
Experimental and Computed EPR *g*-values for WT and βR61A *Re*NHase.

NHase species	Axial ligand	C118-SO_x(H)	Outer-sphere H_2O?	Method	g_1	g_2	g_3	Δg
WT *Re*NHase^{Aq}	H_2O	$CysSO^-$	No	QCT/Taylor	2.257	2.118	1.969	0.288
				Exper.	**2.206**	**2.131**	**1.987**	**0.219**
βR61A *Re*NHase^{Aq}	H_2O	$CysSO^-$	No	QCT/Taylor	2.305	2.141	1.956	0.349
	H_2O	CysSOH	No	QCT/Taylor	2.287	2.125	1.962	0.325
	H_2O	$CysSO^-$	Yes	QCT/Taylor	2.279	2.129	1.963	0.316
				Exper.	**2.248**	**2.142**	**1.998**	**0.250**
WT *Re*NHase^{BA}	CH_3CO_2H	$CysSO^-$	No	QCT/Taylor	2.302	2.126	1.959	0.343
				Exper.	**2.281**	**2.150**	**1.974**	**0.307**
βR61A *Re*NHase^{BA}	$CH_3CO_2^-$	CysSOH	No	QCT/Taylor	2.486	2.125	1.905	0.581
	CH_3CO_2H	CysSOH	No	QCT/Taylor	2.322	2.116	1.956	0.366
	$CH_3CO_2^-$	CysSOH	Yes	QCT/Taylor	2.447	2.116	1.921	0.526
				Exper.	**2.289**	**2.123**	**1.963**	**0.326**
WT *Re*NHase^{Ox}	H_2O	$CysSO_2^-$	No	QCT/Taylor	2.250	2.108	1.972	0.278
				Exper.	**2.180**	**2.114**	**1.998**	**0.182**
βR61A *Re*NHase^{Ox}	H_2O	$CysSO_2^-$	No	QCT/Taylor	2.320	2.126	1.955	0.365
				Exper.	**2.223**	**2.142**	**1.981**	**0.242**

Exper. = experimental data.

work on the Fe-type NHase βR61K mutant enzyme, which also exhibited a blue-shift of ~20 nm [12]. A similar hypsochromic blue shift was also observed when NO or N_3^- was added to an Fe-type NHase. As this LMCT band is due to the axial thiolate ligand donating into the unoccupied e_g* orbital of the Fe(III) center, the observed blue-shift was attributed to greater donation from the axial thiolate cysteine to compensate for the π-accepting nature of the NO or N_3^- [12,14]. For the *Re*NHase βR61A mutant enzyme, the loss of the hydrogen bonding interaction between βR61 and the equatorial sulfenic acid ligand increases the electron density on the ligand, thereby destabilizing the Fe-based 3d orbitals and increasing the energy of the LMCT band. The increase in electron donation to the metal center for both Co- and Fe-type NHases also decreases the Lewis acidity of the active site metal ion, impacting the lability of the axial water molecule and binding affinity of the substrate [16]. These data indicate that the hydrogen bonds from the *Pt*NHase βR52 and *Re*NHase βR61 positions play an important role in tuning the Lewis acidity of the active site metal ion, as well as the nucleophilicity of the sulfenic acid ligand.

The EPR spectrum of WT *Re*NHase corresponds to those previously reported and contains signals from three species: active *Re*NHase (*Re*NHase^{Aq}), inactive and oxidized *Re*NHase (*Re*NHase^{Ox}), and the butyric acid (BA)-bound *Re*NHase (*Re*NHase^{BA}) (Fig. 3A) [23]. The spectrum of *Re*NHase βR61A also contains three species and was simulated using *Re*NHase^{Aq}, *Re*NHase^{Ox}, and *Re*NHase^{BA} (Fig. 3B; Table 3). One species in the EPR spectrum of the *Re*NHase βR61A mutant enzyme, with an isolated peak at 2950 G (g_1 = 2.289) and attributed to the BA complex due to the high value of g_1 and large **g**-anisotropy, is interesting as this resonance is much broader (Δ_{FWHM} ≈ 45 G) than in WT (Δ_{FWHM} ≈ 20 G). The broadening is likely indicative of a less constrained coordination geometry (*g*-strain), consistent with the loss of the second-sphere βR hydrogen bonding interaction. The other two species exhibited low-field resonances at 3000 G (g_1 = 2.248) and 3035 G (g_1 = 2.223), respectively. The g_1 value of 2.223 is close to that (2.206) of WT *Re*NHase^{Aq} but such an assignment would imply a shift in the g_1 value δ*g* of 0.08 for the oxidized species. A more likely explanation is that the g_1 values of both species increased by about 0.04, such that the g_1 = 2.248 species corresponds to the active form and the g_1 = 2.223 species corresponds to the oxidized form of the *Re*NHase βR61A mutant enzyme (Fig. 3C, Table 3).

3.3. X-ray crystal structures of the PtNHase βR52 and βR157 mutant enzymes

X-ray quality, colorless crystals of each of the *Pt*NHase βR mutant enzymes were obtained using identical crystallization conditions to those previously reported for WT *Pt*NHase [2,37]. The lack of any detectable color is consistent with low Co(III) content within the active sites (Table 1). The crystals diffracted between ~1.3 and ~1.6 Å and detailed crystallographic parameters are presented in Table 2. All four X-ray structures confirm the mutations, and their overall structures were nearly identical to the WT *Pt*NHase structure with RMSD ranging from ~0.27 to ~0.45 Å.

The βR157K and βR157A active sites are presented in Fig. 4A and B. No metal density was observed in either active site, so the collected data was solved as the apo-form; however, densities <20% are often poorly resolved via X-ray crystallography so we cannot exclude the possibility of low metal occupancy in the active site. The active site equatorial cysteine ligands αC111 and αC113 are fully reduced in the βR157K structure; each occupies two different orientations in an ~50:50 mixture (Fig. 4A). Substitution of βR157 with Lys allows a single hydrogen bonding interaction, which occurs between the Lys-based N atom and the αC111 sulfur atom (3.8 Å), suggesting a weak hydrogen bonding interaction as the average hydrogen bonding distances between NH and S is 3.5 Å (Fig. 4A, Table 4) [44,45]. Substitution of the βR157 position with Ala removes the hydrogen bonding interaction to the CSD111 ligand that is observed in WT *Pt*NHase (Fig. 1). Interestingly, the structure of the βR157A enzyme revealed that the equatorial αC111 ligand is properly oxidized but, surprisingly, the axial αC108 ligand is partially oxidized to αCSO108 (~50%) (Fig. 4B). The other equatorial αC113 ligand is fully reduced (Fig. 4B). For the βR157A structure, an hydrogen bond from the primary amine to an oxygen atom of the oxidized αCSD111 ligand is observed (3.2 Å; Fig. 4B) and also to the reduced equatorial αC113 ligand sulfur atom (3.6 Å) (Fig. 4B). However, an hydrogen bond is not observed between the secondary amine of βR52 and the αCSD111 equatorial ligand, which is observed in the WT structure (Fig. 1) as its too far from the secondary amine of βR52 (4.0 Å, Table 4). It is unclear why the αCSD111 and αC108 ligands are oxidized in the βR157A mutant enzyme but not in the βR157K structure. Understanding this oxidation is complicated by the proposed subunit swapping mechanism, but an appealing explanation is the loss of salt bridge formation, which impedes active site maturation and consequently subunit swapping. This explanation is also consistent with the depletion of cobalt in the active site of both βR157A and βR157K structures. Then, perhaps, in the absence of any hydrogen bonds, the αC111 sulfur is more susceptible to oxidation, as the redox potential of a cysteine ligand would be impacted with the loss of the βR hydrogen bonding interactions [46,47]. Taken together, these data further support the proposal that βR157 plays a role in the proposed subunit swapping mechanism.

As the second-sphere βR52 residue forms hydrogen bonds with both the αCSD111 and αCSO113 acid ligands in the WT *Pt*NHase structure (Fig. 1), the latter of which functions as the nucleophile during catalytic

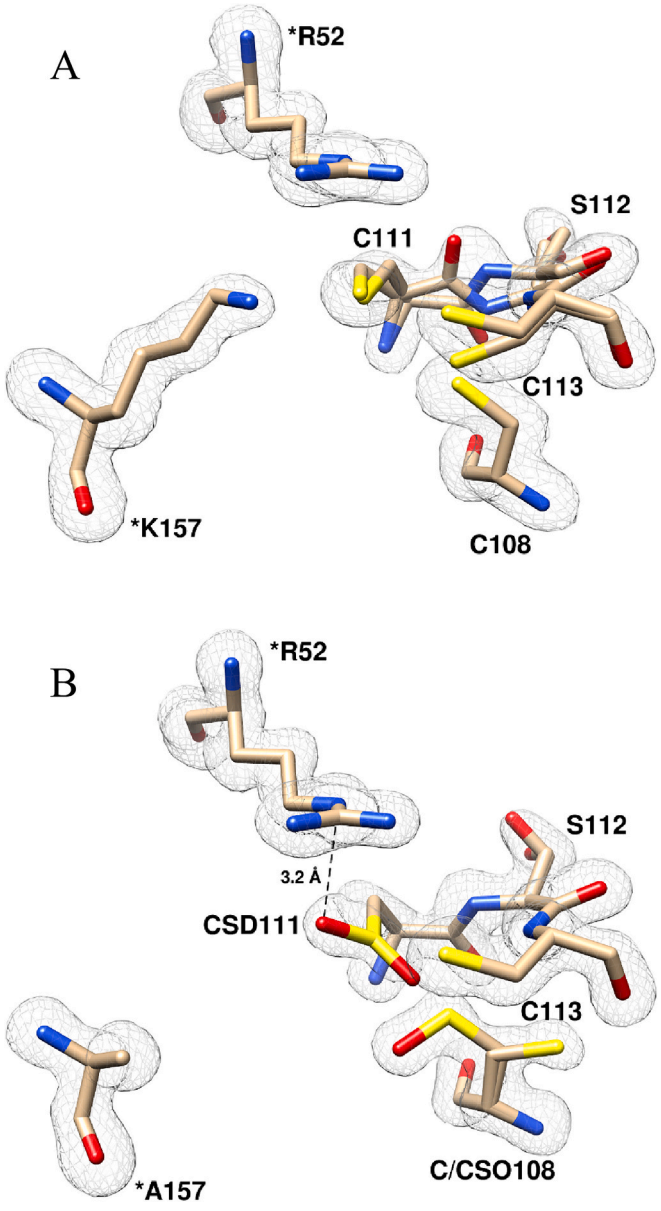

Fig. 4. **A**) Active site of βR157K with second-sphere 52 and 157 positions from the β-subunit shown. No metal was observed in the active site. Residues from the β-subunit are denoted with an *. Only hydrogen-bonding distances (<3.5 Å) are shown. αCys111, αSer112 and αCys113 are built in two alternate conformers respectively based on electron density (Polder map at 4.5 sigma level). **B**) Active site of βR157A with second-sphere 52 and 157 positions from the β-subunit shown. No metal was observed in the active site. Residues from the β-subunit are denoted with an *. Key hydrogen bonding distances between the α and β subunits are shown in Å. αCys108 and αSer112 are built in two alternate conformers respectively based on electron density (Polder map at 4.0 sigma level). One of the alternate conformers of αCys108 is modeled as sulfenic acid (CSO). αCys111 is modeled as sulfinic acid (CSD).

turnover, mutation of the βR52 residue to a K or A residue provides insight into the catalytic mechanism as well as the subunit swapping mechanism. Interestingly, in the βR52K structure, neither of the active site equatorial αCys ligands (αC111 and αC113) are oxidized, similar to the βR157K structure (Fig. 5A); however, two different αC108, αC111, and αC113 sulfur atom conformations are observed in an ~60:40 ratio. Hydrogen bonds are observed between the βR52K primary amine N atom and the αC111 sulfur atom (3.3 Å) and the αC113 sulfur atom (3.1 Å). Substitution of βR52 with an A residue, which eliminates hydrogen bonding, results in the αC113 ligand being partially oxidized to αCSO113 (~60%) but the αC111 ligand remains fully reduced (Fig. 5B). It is also notable that the αC113 ligand is oxidized in the βR52A structure but not in the βR52K structure, which is the opposite to that observed for the βR157A structure. This observation supports the suggestion that the salt bridges proposed to form between the βR157 and βR52 residues with the $\alpha\varepsilon_2$ complex are important for the post-translational maturation of the NHase active site as well as the subunit swapping process.

Table 4
Hydrogen bonding distances between first- and second-sphere ligands with distances in Å.

Bonds	Species					
	WT	APO-WT	R52K	R52A	R157K	R157A
R157/K157 Primary NH_2 – S-C111	3.9	3.3	–	3.3	3.8	–
R157 Secondary NH_2 – S-C111	4.0	4.0	–	2.8	–	–
R52/K52 Primary NH_2 –S-C111	–	4.7	3.3	–	4.3	4.6
R52/K52 Primary NH_2 – S-C113	3.8	5.4	3.1	–	3.7	3.6
R52 Secondary NH_2 – S-C111	3.9	4.1	–	–	3.8	4.0
R52 Secondary NH_2 – O-CSD111	2.8	–	–	–	–	3.2

WT *Pt*NHase (PDB: 1IRE) and Apo-WT *Pt*NHase (PDB: 1UGQ) [2,37].

3.4. Computational studies

Additional insights into the spectroscopic and crystallographic features of the NHase active site were obtained using computational methods. Our previous studies of WT *Re*NHase determined that the functional active site (*Re*NHase^{Aq}) features a six-coordinate Fe(III) center bound to an axial H_2O ligand, which participates in hydrogen bonding interactions with the anionic (i.e., unprotonated) αCSO118 and αCSD116 donors [23]. Removal of the βR61 residue in silico, followed by constrained geometry reoptimization using DFT, causes only minor changes in the overall structure; however, it's clear that loss of the βR61 residue strengthens the hydrogen bond between the axial H_2O ligand and the deprotonated αCSO118 ligand, as evident in the shortening of the αCSO118 anion SO···H_2O distance (from 1.61 in WT to 1.47 Å in βR61A) and elongation of the O—H bond by 0.04 Å. Thus, it appears that eliminating the hydrogen bond with the second-sphere $\beta R61^+$ residue causes the deprotonated αCSO118 ligand to become significantly more basic in the βR61A variant. This conclusion is further supported by DFT calculations of the BA-bound *Re*NHase βR61A mutant enzyme (*Re*NHase^{BA}), in which the BA molecule is truncated to acetic acid in DFT calculations for simplicity. In the WT enzyme, the carboxylic acid of BA coordinates as a neutral ligand, stabilized by hydrogen bonding between the carboxylate (CO_2H) functional group and the αCSO118 anionic ligand. Interestingly, geometry optimizations of the βR61A site converge to a structure featuring an acetate ligand and a protonated αCSO118 unit (Fig. 6).

Based on these data, active-site structures of the *Re*NHase βR61A mutant enzyme in which removal of βR61 is accompanied by protonation of the anionic αCSO118 ligand to give the protonated αCSO118 form, were also considered. In the resulting *Re*NHase^{Aq} model, a weak hydrogen bond is established between the adjacent protonated αCSO118 and the αCSD116 anion ligands during geometry optimization, which reduces the (O_2)S-Fe-S(OH) angle from 94.3° (in WT) to 89.6°. Protonation also disrupts the hydrogen bond between αCSO118 and the axial H_2O ligand that is observed in both WT and unprotonated βR61A structures. Not surprisingly, the protonated αCSO118 group is incapable of deprotonating the carboxylic acid moiety of the BA-bound model of

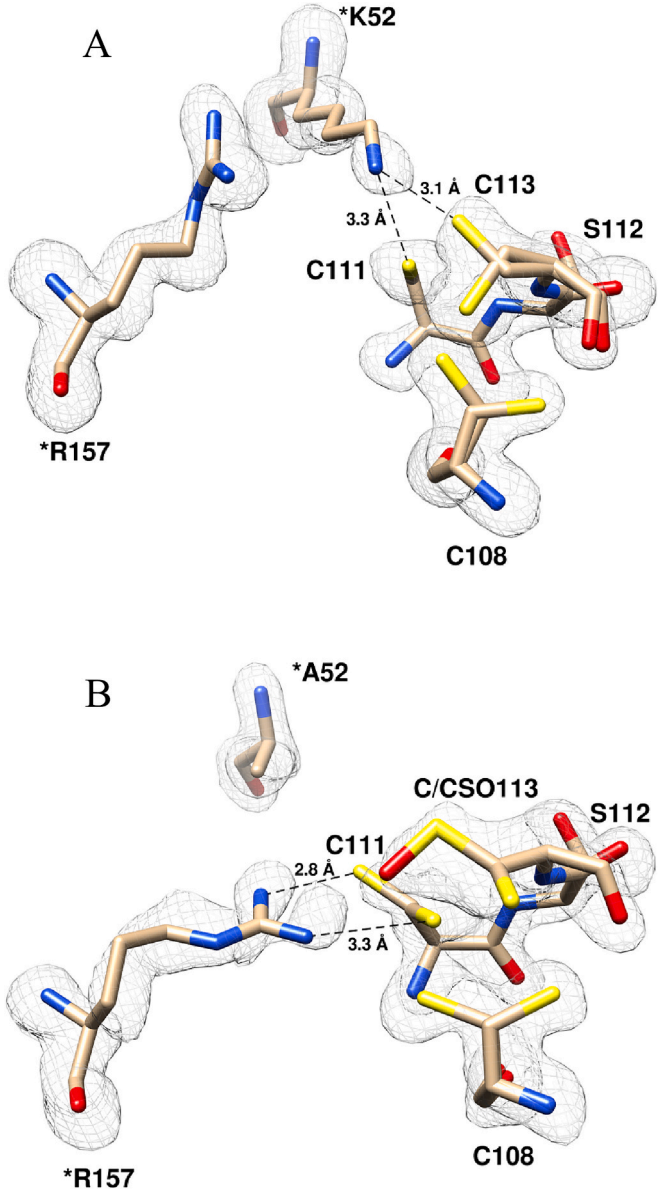

Fig. 5. **A**) Active site of βR52K with second-sphere 52 and 157 positions from the β-subunit are shown. No metal was observed in the active site. Residues from β subunit are denoted with an *. Key hydrogen bonding distances between α and β-subunit residues are shown in Å. αCys108 and αCys113 are built in two alternate conformers respectively based on electron density (Polder map at 3.0 sigma level). **B**) Active site of βR52A with second-sphere 52 and 157 positions from the β subunit are shown. No metal was observed in the active site. Residues from the β-subunit are denoted with an *. Key hydrogen-bonding distances between α and β-subunit residues are shown in Å. αCys108, αCys111, αSer112 and αCys113 are built in two alternate conformers respectively based on electron density (Polder map at 3.0 sigma level).

βR61A. Instead, the resulting structure features a hydrogen bond between the neutral CH_3CO_2H and αCSO118 ligands, similar to the arrangement found in WT models of *Re*NHase^{BA}. Finally, active-site models of *Re*NHase βR61A that contain an adventitious H_2O molecule in the space formerly occupied by βR61 were generated. After geometry optimization, the added H_2O assumes a position in the optimized structures that maximizes hydrogen bonding interactions with both the αCSO118 and αCSD116 donors. In the BA-bound structure, the model optimizes to a structure featuring an anionic carboxylic acid ligand and protonated αCSO118 unit, suggesting that the outer-sphere H_2O molecule does not fully compensate for loss of hydrogen bonding from the βR61 residue.

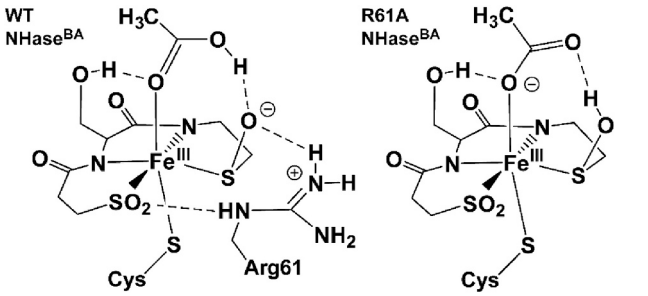

Fig. 6. Changes in ligand protonation states in DFT models of the *Re*NHase^{BA} active site.

Calculations of EPR *g*-values were also used to assess the relative validity of these competing models of the WT *Re*NHase and the *Re*NHase βR61A active sites. As described in the Computational Methods section, quantum chemical theory (QCT) based on ab initio CASSCF/NEVPT2 calculations were used to determine the relative energies of the three lowest energy ligand-field states, which are derived from the parent $^2T_{2g}$ state in octahedral symmetry. According to the theoretical framework developed by Taylor and others, the mixing of these states via spin-orbit coupling (SOC) is responsible for the anisotropy of the **g**-tensor [34,35]. Table 3 compares experimental *g*-values to those computed using QCT for different *Re*NHase active-site models. The combined QCT/Taylor approach tends to overestimate the overall anisotropy of the **g**-tensor, defined as $\Delta g = g_1 - g_3$, by 0.05–0.10. Yet the calculations accurately reproduce the trend in *g*-anisotropy across the WT series, which follows the order *Re*NHase^{BA} > *Re*NHase^{Aq} > *Re*NHase^{Ox}. Significantly, the computed *g*-values of the three βR61A *Re*NHase^{Aq} models are each slightly more anisotropic than the WT model, consistent with the shifts observed experimentally upon removal of βR61 (Table 3). The best agreement with experiment is provided by *Re*NHase^{Aq} models in which the αCSO118 ligand is either protonated (αCSO118-SOH) or hydrogen bonded to an outer-sphere H_2O molecule (αCSO118-SO^-/H_2O), although the variations of computed *g*-values across the βR61A *Re*NHase^{Aq} series are fairly small.

More dramatic differences are observed between the computed **g**-tensors of βR61A *Re*NHase^{BA} models. Those containing an axial carboxylate anion ($CH_3CO_2^-$) yielded computed g_1-values of 2.49 and 2.45 (Table 3), far greater than the experimental g_1-value of 2.289. Thus, based on the computational data, deprotonation of the BA-derived ligand in the βR61A *Re*NHase^{BA} active site is expected to be accompanied by large changes in the EPR spectrum, which is not observed experimentally. Instead, better agreement with experiment is observed for the βR61A *Re*NHase^{BA} model that features a neutral carboxylic acid and a protonated αCSO118 ligand ($g_1 = 2.322$). The computed **g**-tensor of this model is only slightly more anisotropic than the corresponding WT tensor, which is consistent with the minor shifts in *g*-values observed experimentally between WT and βR61A *Re*NHase^{BA}.

Collectively, our computational results suggest that the deprotonated αCSO118 unit of *Re*NHase may compensate for the loss of the βR61 residue by gaining a proton to generate a protonated αCSO118 ligand. Because the O-atom of αCSO118 engages in nucleophilic attack of the nitrile substrate in the NHase mechanism, protonation of this ligand may account for the lack of activity of the βR61A mutants (Fig. 6). A neutral αCSO118 moiety would be far less nucleophilic than an anionic αCSO118 unit, thereby hindering formation of the proposed cyclic intermediate. Thus, the second-sphere βR61 residue likely facilitates catalysis by stabilizing the αCSO118 ligand in its deprotonated (anionic) state via hydrogen bonding interactions.

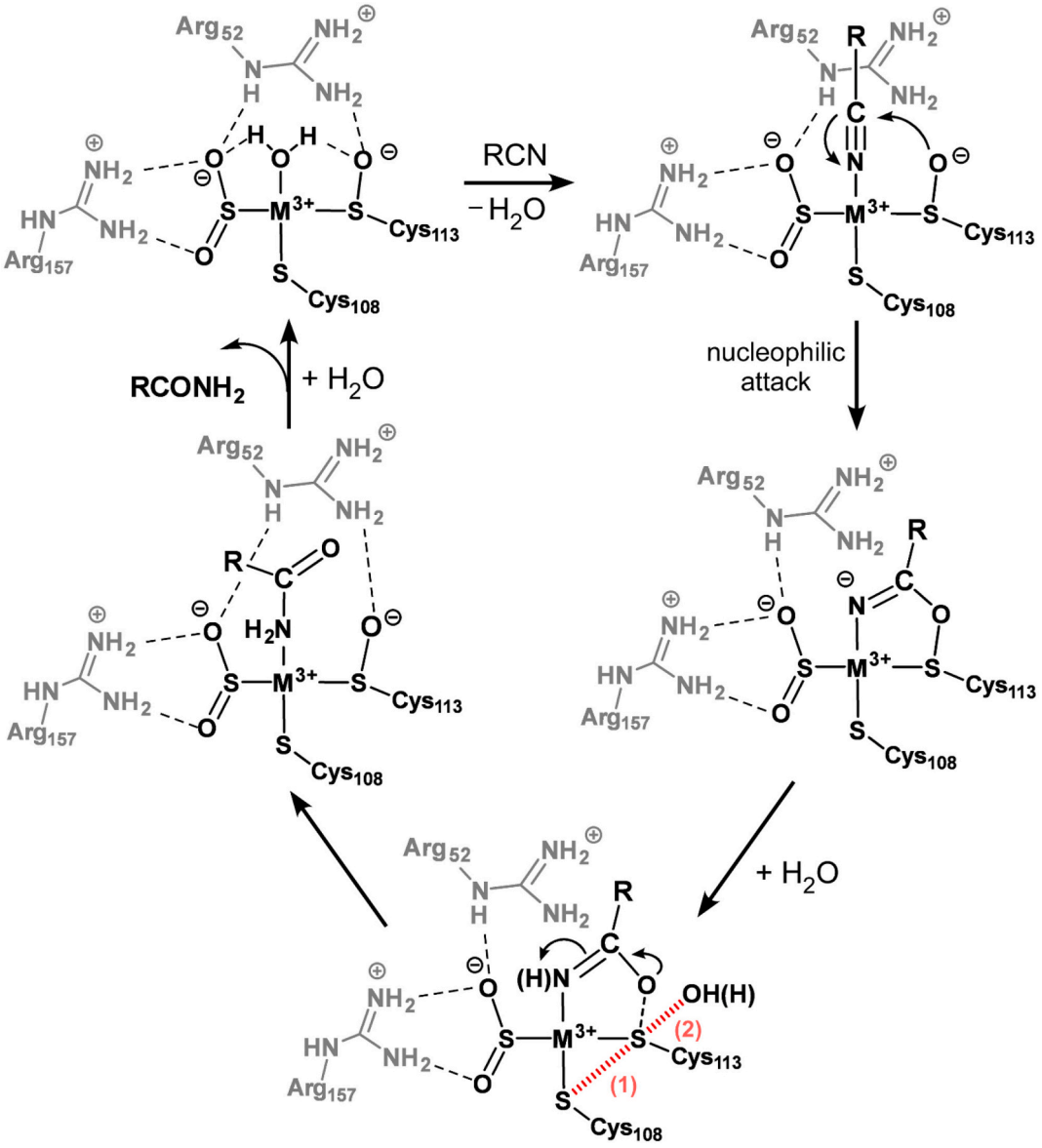

Fig. 7. Proposed mechanism of catalysis, consistent with previous publications, with the second-sphere arginine residues included. Red hashed lines indicate potential stabilizing disulfide bond (1) or the stabilization of the sulfur through the reformation of the sulfenic acid with a water molecule (2). Ligand numbering refers to *Pt*NHase system. (For interpretation of the references to color in this figure legend, the reader is referred to the web version of this article.)

4. Conclusions

The data described herein supports the proposed salt bridge formation between the two highly conserved, positively charged second-sphere active site βR residues and the negatively charged active site equatorial sulfenic/sulfinic acid ligands in the α-subunit of the $\alpha\varepsilon_2$ complex, which drives subunit swapping [9–11]. Additionally, these data support the previously proposed catalytic mechanism for NHases and lend new insights into the second-sphere hydrogen bonding network that is integral to catalysis. Specifically, the hydrogen bond from the βR52 and βR61 positions in *Pt*NHase and *Re*NHase, respectively, tune the Lewis acidity of the active site metal ion as well as the basicity of the sulfenic acid ligand. The combination of DFT calculations, EPR spectroscopy and X-ray crystallographic data reported herein support the suggestion that both of the sulfenic and sulfinic acid ligands are deprotonated in the active enzyme, and that the anionic forms are stabilized by hydrogen bonds from the conserved second-sphere βR residues. As the O-atom of the sulfenic acid ligand (SO^-) is required to function as the nucleophile in the catalytic mechanism, protonation of the sulfenic acid (SOH) ligand may account for the lack of activity of the βR52/61Ala mutant enzymes.

These findings allow the proposed catalytic mechanism to be updated to include two integral second-sphere residues (Fig. 7). Salient features of the proposed mechanism that remain the same include (i) direct coordination of the nitrile substrate to the active site metal center activating the nitrile bond towards nucleophilic attack, (ii) nucleophilic attack of the bound nitrile carbon by the sulfenic acid ligand, forming a cyclic intermediate, and (iii) the transfer of two protons upon product release, which is the rate-limiting step based on kinetic isotope studies [14,48]. The anionic and deprotonated nucleophilic equatorial sulfenic acid ligand is stabilized in the more nucleophilic -SO^- form through the hydrogen bonding of βR52 in *Pt*NHase and βR61 in *Re*NHase. After nucleophilic attack, once the cyclic intermediate is formed, tautomerization occurs to form the iminol. This intermediate state necessitates stabilization of a reduced αC113 ligand, which has been proposed to occur either through a disulfide bond intermediate or through a water molecule that reforms the sulfenic-αC113 ligand (shown through red hashed lines in Fig. 7) [16]. The suggested disulfide intermediate has

only been proposed from theoretical studies. Time-resolved X-ray crystallographic studies failed to detect a disulfide species, and mutation of the axial Cys ligand to His still resulted in active enzyme [16]. Therefore, the formation of a disulfide bond between the axial Cys ligand and the equatorial sulfenic acid is not catalytically required. However, a recent EPR study reported a catalytically relevant intermediate that was tentatively assigned to a disulfide intermediate [22]. Finally, when the amide product is released and the nucleophilic sulfenic acid is reformed, the second-sphere βR52 residue is able to stabilize the αCSO113 anion through hydrogen bonding. Therefore, both second-sphere arginine residues are important in stabilizing the equatorial cysteine ligands in their oxidized and deprotonated forms, which is essential for catalysis. This work also confirms the necessity of the conserved second-sphere βR residues for the subunit swapping process and post-translational modification of the α-subunit in the $\alpha\varepsilon_2$ complex along with stabilizing the catalytic nucleophile, αCSO113, in its anionic form through hydrogen bonding.

CRediT authorship contribution statement

Callie Miller: Writing – review & editing, Writing – original draft, Validation, Methodology, Investigation, Formal analysis, Data curation. **Delanie Huntoon:** Investigation, Formal analysis, Data curation. **Nicholas Kaley:** Formal analysis, Data curation. **Irene Ogutu:** Writing – review & editing, Validation, Methodology, Investigation, Formal analysis, Data curation, Conceptualization. **Adam T. Fiedler:** Writing – review & editing, Project administration, Methodology, Investigation, Funding acquisition, Formal analysis. **Brian Bennett:** Writing – review & editing, Writing – original draft, Project administration, Methodology, Investigation, Funding acquisition, Formal analysis, Data curation, Conceptualization. **Dali Liu:** Writing – review & editing, Investigation, Formal analysis, Data curation. **Richard Holz:** Writing – review & editing, Validation, Supervision, Resources, Project administration, Methodology, Investigation, Funding acquisition, Formal analysis, Data curation, Conceptualization.

Declaration of competing interest

The authors declare that they have no known competing financial interests or personal relationships that could have appeared to influence the work reported in this paper.

Data availability

Data will be made available on request.

Acknowledgement

This work is supported by the National Science Foundation, CHE-2204024 and CHE-1808711, the Todd Wehr Foundation, Bruker Biospin, and the National Institutes of Health/NIBIB National Biomedical EPR Center (P41-EB001980). We thank Dr. Annette Erbse (University of Colorado Boulder) for providing access to the circular dichroism facilities.

Appendix A. Supplementary data

The manuscript is accompanied by Supporting Information which contains a scheme of the proposed subunit swapping process, the DFT geometry-optimized model of WT NHase^{Aq}, circular dichroism spectra of WT and βR61A *Re*NHase, and UV–Vis absorbance spectra of the *Pt*NHase mutants. Supplementary data to this article can be found online at [https://doi.org/10.1016/j.jinorgbio.2024.112565].

References

[1] A. Chang, L. Jeske, S. Ulbrich, J. Hofmann, J. Koblitz, I. Schomburg, M. Neumann-Schaal, D. Jahn, D. Schomburg, BRENDA, the ELIXIR core data resource in 2021: New developments and updates, Nucleic Acids Res. 49 (2021) D498–D508, https://doi.org/10.1093/nar/gkaa1025.

[2] A. Miyanaga, S. Fushinobu, K. Ito, T. Wakagi, Crystal structure of cobalt-containing nitrile hydratase, Biochem. Biophys. Res. Commun. (2001), https://doi.org/10.1006/bbrc.2001.5897.

[3] K.M. Light, Y. Yamanaka, M. Odaka, E.I. Solomon, Spectroscopic and computational studies of nitrile hydratase: insights into geometric and electronic structure and the mechanism of amide synthesis, Chem. Sci. (2015), https://doi.org/10.1039/c5sc02012c.

[4] A. Dey, M. Chow, K. Taniguchi, P. Lugo-Mas, S. Davin, M. Maeda, J.A. Kovacs, M. Odaka, K.O. Hodgson, B. Hedman, E.I. Solomon, Sulfur K-edge XAS and DFT calculations on nitrile hydratase: geometric and electronic structure of the non-heme iron active site, J. Am. Chem. Soc. (2006), https://doi.org/10.1021/ja0549695.

[5] T. Noguchi, M. Nojiri, K.I. Takei, M. Odaka, N. Kamiya, Protonation structures of Cys-sulfinic and Cys-sulfenic acids in the photosensitive nitrile hydratase revealed by Fourier transform infrared spectroscopy, Biochemistry (2003), https://doi.org/10.1021/bi035260i.

[6] M. Nojiri, M. Yohda, M. Odaka, Y. Matsushita, M. Tsujimura, T. Yoshida, N. Dohmae, K. Takio, I. Endo, Functional expression of nitrile hydratase in Escherichia coli: requirement of a nitrile hydratase activator and post-translational modification of a ligand cysteine, J. Biochem. (1999), https://doi.org/10.1093/oxfordjournals.jbchem.a022339.

[7] Y. Xia, Z. Cheng, C. Hou, L. Peplowski, Z. Zhou, X. Chen, Discovery of the ATPase activity of a cobalt-type nitrile hydratase activator and its promoting effect on enzyme maturation, Biochemistry Article AS (2022), https://doi.org/10.1021/acs.biochem.2c00167.

[8] Y. Xia, L. Peplowski, Z. Cheng, T. Wang, Z. Liu, W. Cui, M. Kobayashi, Z. Zhou, Metallochaperone function of the self-subunit swapping chaperone involved in the maturation of subunit-fused cobalt-type nitrile hydratase, Biotechnol. Bioeng. (2019), https://doi.org/10.1002/bit.26865.

[9] Z. Zhou, Y. Hashimoto, K. Shiraki, M. Kobayashi, Discovery of posttranslational maturation by self-subunit swapping, Proc. Natl. Acad. Sci. USA (2008), https://doi.org/10.1073/pnas.0803428105.

[10] Z. Zhou, Y. Hashimoto, M. Kobayashi, Self-subunit swapping chaperone needed for the maturation of multimeric metalloenzyme nitrile hydratase by a subunit exchange mechanism also carries out the oxidation of the metal ligand cysteine residues and insertion of cobalt, J. Biol. Chem. (2009), https://doi.org/10.1074/jbc.M808464200.

[11] Z. Zhou, Y. Hashimoto, T. Cui, Y. Washizawa, H. Mino, M. Kobayashi, Unique biogenesis of high-molecular mass multimeric metalloenzyme nitrile hydratase: intermediates and a proposed mechanism for self-subunit swapping maturation, Biochemistry (2010), https://doi.org/10.1021/bi100651v.

[12] S.R. Piersma, M. Nojiri, M. Tsujimura, T. Noguchi, M. Odaka, M. Yohda, Y. Inoue, I. Endo, Arginine 56 mutation in the β subunit of nitrile hydratase: importance of hydrogen bonding to the non-heme iron center, J. Inorg. Biochem. (2000), https://doi.org/10.1016/S0162-0134(00)00076-3.

[13] I.R.A.M. Ogutu, R.C. Holz, B. Bennett, Insight into the maturation process of the nitrile hydratase active site, Inorg. Chem. (2021), https://doi.org/10.1021/acs.inorgchem.0c02924.

[14] N. Gumataotao, M.L. Kuhn, N. Hajnas, R.C. Holz, Identification of an active site-bound nitrile hydratase intermediate through single turnover stopped-flow spectroscopy, J. Biol. Chem. (2013), https://doi.org/10.1074/jbc.M112.398909.

[15] S. Martinez, R. Wu, R. Sanishvili, D. Liu, R. Holz, The active site sulfenic acid ligand in nitrile hydratases can function as a nucleophile, J. Am. Chem. Soc. (2014), https://doi.org/10.1021/ja410462j.

[16] I.R.A.M. Ogutu, M.St. Maurice, B. Bennett, R.C. Holz, Examination of the catalytic role of the axial cystine ligand in the co-type nitrile hydratase from pseudonocardia thermophila JCM 3095, Catalysts (2021), https://doi.org/10.3390/catal11111381.

[17] S. Martinez, M.L. Kuhn, J.T. Russell, R.C. Holz, T.E. Elgren, Acrylamide production using encapsulated nitrile hydratase from Pseudonocardia thermophila in a sol–gel matrix, J. Mol. Catal. B Enzym. 100 (2014) 19–24, https://doi.org/10.1016/j.molcatb.2013.11.014.

[18] K.P.W. Lankathilaka, N. Stein, R.C. Holz, B. Bennett, Cellular maturation of an iron-type nitrile hydratase interrogated using EPR spectroscopy, JBIC J. Biol. Inorg. Chem. 24 (2019) 1105–1113, https://doi.org/10.1007/s00775-019-01720-y.

[19] A.J. Miles, S.G. Ramalli, B.A. Wallace, <scp>DichroWeb</scp>, a website for calculating protein secondary structure from circular dichroism spectroscopic data, Protein Sci. 31 (2022) 37–46, https://doi.org/10.1002/pro.4153.

[20] The Mathworks Inc., MATLAB - MathWorks. http://www.mathworks.com/products/matlab, 2016.

[21] S. Stoll, A. Schweiger, EasySpin, a comprehensive software package for spectral simulation and analysis in EPR, J. Magn. Reson. (2006), https://doi.org/10.1016/j.jmr.2005.08.013.

[22] W.L. Karunagala Pathiranage, N. Gumataotao, A.T. Fiedler, R.C. Holz, B. Bennett, Identification of an intermediate species along the nitrile hydratase reaction pathway by EPR spectroscopy, Biochemistry (2021), https://doi.org/10.1021/acs.biochem.1c00574.

[23] N. Stein, N. Gumataotao, N. Hajnas, R. Wu, K.P.W. Lankathilaka, U.T. Bornscheuer, D. Liu, A.T. Fiedler, R.C. Holz, B. Bennett, Multiple states of nitrile hydratase from Rhodococcus equi TG328-2: structural and mechanistic insights from Electron

paramagnetic resonance and density functional theory studies, Biochemistry (2017), https://doi.org/10.1021/acs.biochem.6b00876.
[24] F. Neese, The ORCA program system, WIREs Comput Mol. Sci. 2 (2012) 73–78, https://doi.org/10.1002/wcms.81.
[25] F. Neese, Software update: the ORCA program system, version 4.0, WIREs Comput Mol. Sci. 8 (2018), https://doi.org/10.1002/wcms.1327.
[26] F. Weigend, R. Ahlrichs, Balanced basis sets of split valence, triple zeta valence and quadruple zeta valence quality for H to Rn: design and assessment of accuracy, Phys. Chem. Chem. Phys. 7 (2005) 3297, https://doi.org/10.1039/b508541a.
[27] F. Weigend, Accurate coulomb-fitting basis sets for H to Rn, Phys. Chem. Chem. Phys. 8 (2006) 1057, https://doi.org/10.1039/b515623h.
[28] J.P. Perdew, K. Burke, M. Ernzerhof, Generalized gradient approximation made simple, Phys. Rev. Lett. 77 (1996) 3865–3868, https://doi.org/10.1103/PhysRevLett.77.3865.
[29] F. Neese, Prediction of electron paramagnetic resonance *g* values using coupled perturbed Hartree–Fock and Kohn–Sham theory, J. Chem. Phys. 115 (2001) 11080–11096, https://doi.org/10.1063/1.1419058.
[30] F. Neese, Quantum chemical calculations of spectroscopic properties of metalloproteins and model compounds: EPR and Mössbauer properties, Curr. Opin. Chem. Biol. 7 (2003) 125–135, https://doi.org/10.1016/S1367-5931(02)00006-6.
[31] C. Angeli, R. Cimiraglia, S. Evangelisti, T. Leininger, J.-P. Malrieu, Introduction of *n* -electron valence states for multireference perturbation theory, J. Chem. Phys. 114 (2001) 10252–10264, https://doi.org/10.1063/1.1361246.
[32] S.K. Singh, M. Atanasov, F. Neese, Challenges in multireference perturbation theory for the calculations of the *g* -tensor of first-row transition-metal complexes, J. Chem. Theory Comput. 14 (2018) 4662–4677, https://doi.org/10.1021/acs.jctc.8b00513.
[33] A.A. Fischer, J.R. Miller, R.J. Jodts, D.M. Ekanayake, S.V. Lindeman, T.C. Brunold, A.T. Fiedler, Spectroscopic and computational comparisons of thiolate-ligated ferric Nonheme complexes to cysteine dioxygenase: second-sphere effects on substrate (analogue) positioning, Inorg. Chem. 58 (2019) 16487–16499, https://doi.org/10.1021/acs.inorgchem.9b02432.
[34] C.P.S. Taylor, The EPR of low spin heme complexes relation of the τ2g hole model to the directional properties of the g tensor, and a new method for calculating the ligand field parameters, Biochim. et Biophys. Acta (BBA) - Protein Struct. 491 (1977) 137–148, https://doi.org/10.1016/0005-2795(77)90049-6.
[35] J.S. Griffith, Binding in Hæmoglobin Azide as determined by Electron resonance: theory of Electron resonance in Ferrihæmoglobin Azide, Nature 180 (1957) 30–31, https://doi.org/10.1038/180030a0.
[36] P. Lugo-Mas, A. Dey, L. Xu, S.D. Davin, J. Benedict, W. Kaminsky, K.O. Hodgson, B. Hedman, E.I. Solomon, J.A. Kovacs, How does single oxygen atom addition affect the properties of an Fe−nitrile hydratase analogue? The compensatory role of the unmodified thiolate, J. Am. Chem. Soc. 128 (2006) 11211–11221, https://doi.org/10.1021/ja062706k.
[37] A. Miyanaga, S. Fushinobu, K. Ito, H. Shoun, T. Wakagi, Mutational and structural analysis of cobalt-containing nitrile hydratase on substrate and metal binding, Eur. J. Biochem. (2004), https://doi.org/10.1046/j.1432-1033.2003.03943.x.
[38] C. Vonrhein, C. Flensburg, P. Keller, A. Sharff, O. Smart, W. Paciorek, T. Womack, G. Bricogne, Data processing and analysis with the *autoPROC* toolbox, Acta Crystallogr. D Biol. Crystallogr. 67 (2011) 293–302, https://doi.org/10.1107/S0907444911007773.
[39] G. Bunkóczi, N. Echols, A.J. McCoy, R.D. Oeffner, P.D. Adams, R.J. Read, *Phaser. MRage* : automated molecular replacement, Acta Crystallogr. D Biol. Crystallogr. 69 (2013) 2276–2286, https://doi.org/10.1107/S0907444913022750.
[40] D. Liebschner, P.V. Afonine, M.L. Baker, G. Bunkóczi, V.B. Chen, T.I. Croll, B. Hintze, L.-W. Hung, S. Jain, A.J. McCoy, N.W. Moriarty, R.D. Oeffner, B.K. Poon, M.G. Prisant, R.J. Read, J.S. Richardson, D.C. Richardson, M.D. Sammito, O. V. Sobolev, D.H. Stockwell, T.C. Terwilliger, A.G. Urzhumtsev, L.L. Videau, C. J. Williams, P.D. Adams, Macromolecular structure determination using X-rays, neutrons and electrons: recent developments in *Phenix*, Acta Crystallogr. D Struct. Biol. 75 (2019) 861–877, https://doi.org/10.1107/S2059798319011471.
[41] E.F. Pettersen, T.D. Goddard, C.C. Huang, G.S. Couch, D.M. Greenblatt, E.C. Meng, T.E. Ferrin, UCSF chimera—a visualization system for exploratory research and analysis, J. Comput. Chem. 25 (2004) 1605–1612, https://doi.org/10.1002/jcc.20084.
[42] K. Hashimoto, H. Suzuki, K. Taniguchi, T. Noguchi, M. Yohda, M. Odaka, Catalytic mechanism of nitrile hydratase proposed by time-resolved X-ray crystallography using a novel substrate, tert-butylisonitrile, J. Biol. Chem. (2008), https://doi.org/10.1074/jbc.M806577200.
[43] S. Martinez, X. Yang, B. Bennett, R.C. Holz, A cobalt-containing eukaryotic nitrile hydratase, Biochim. Biophys. Acta, Proteins Proteomics (2017), https://doi.org/10.1016/j.bbapap.2016.09.013.
[44] H.S. Biswal, S. Wategaonkar, Nature of the N−H···S hydrogen bond, J. Phys. Chem. A 113 (2009) 12763–12773, https://doi.org/10.1021/jp907658w.
[45] A. Lautié, A. Novak, N-H.S hydrogen bonds, Chem. Phys. Lett. 71 (1980) 290–293, https://doi.org/10.1016/0009-2614(80)80166-7.
[46] A.J. McGrath, G.E. Garrett, L. Valgimigli, D.A. Pratt, The redox chemistry of Sulfenic acids, J. Am. Chem. Soc. 132 (2010) 16759–16761, https://doi.org/10.1021/ja1083046.
[47] P. Hosseinzadeh, Y. Lu, Design and fine-tuning redox potentials of metalloproteins involved in electron transfer in bioenergetics, Biochim. et Biophys. Acta (BBA) - Bioenerget. 1857 (2016) 557–581, https://doi.org/10.1016/j.bbabio.2015.08.006.
[48] S. Mitra, R.C. Holz, Unraveling the catalytic mechanism of nitrile hydratases, J. Biol. Chem. (2007), https://doi.org/10.1074/jbc.M604117200.
[49] N. Gumataotao, K.P.W. Lankathilaka, B. Bennett, R.C. Holz, The iron type nitrile hydratase activator protein is a GTPase, Biochem. J. 474 (2017) 247–258, https://doi.org/10.1042/BCJ20160884.